

# **Modeling Discharge and Charge Characteristics of Nickel-Metal Hydride Batteries**

W.B. Gu and C.Y. Wang\*

Department of Mechanical Engineering & Pennsylvania Transportation Institute  
The Pennsylvania State University  
University Park, PA 16802, USA

S.M. Li

Department of Mechanical Engineering  
University of Hawaii at Manoa  
Honolulu, HI 96822, USA

M.M. Geng and B.Y. Liaw  
Hawaii Natural Energy Institute  
University of Hawaii at Manoa  
Honolulu, HI 96822, USA

Submitted to *Electrochimica Acta*  
November 1998

---

\* corresponding Author. Email: cxw31@psu.edu

**Abstract**—A combined numerical and experimental study of the discharge and charge of nickel-metal hydride (Ni-MH) batteries has been performed. Numerical simulations were based on a previously developed micro-macroscopic coupled model which includes both the proton diffusion in the nickel active material and the hydrogen diffusion in metal-hydride particles. Oxygen generation and recombination, a principal mechanism to ensure safe operation of Ni-MH cells during overcharge, is also accounted for. A sealed Ni-MH cell (AA size, 1Ah capacity) was prepared and discharge experiments were conducted at various rates. These experimental data along with other discharge and charge data available in the literature were used to validate the present model. Numerical results were presented to show the effects of oxygen evolution on battery performance, particularly on the charge acceptance, cell pressure build-up, and self-discharge. This combined experimental and numerical study yields a computer-aided tool for the design and optimization of Ni-MH batteries.

*Key words:* nickel-metal hydride battery, oxygen reaction, modeling and computer simulation

## LIST OF SYMBOLS

$a$	specific interfacial area, $\text{cm}^2/\text{cm}^3$
$c^i$	volume-averaging concentration of species $i$ over a phase, $\text{mol}/\text{cm}^3$
$\bar{c}^i$	area-averaging concentration of species $i$ at an interface, $\text{mol}/\text{cm}^3$
$D^i$	diffusion coefficient of species $i$ , $\text{cm}^2/\text{s}$
$F$	Faraday's constant, $96,487 \text{ C}/\text{mol}$
$f_{\pm}$	mean molar activity coefficient of the electrolyte
$H$	Henry constant for $\text{O}_2$ -KOH aqueous solution system, $\text{mol}/\text{cm}^3 \cdot \text{atm}$
$I$	current density, $\text{A}/\text{cm}^2$
$\bar{i}_{nj}$	transfer current density of reaction $j$ , $\text{A}/\text{cm}^2$
$i_{0j,\text{ref}}$	exchange current density of reaction $j$ at the reference conditions, $\text{A}/\text{cm}^2$
$j^i$	reaction current density resulting in production or consumption of species $i$ , $\text{A}/\text{cm}^3$
$K$	interfacial mass transfer coefficient, $1/\text{s}$
$k$	intercalation constant of nickel electrode
$L$	cell width, $\text{cm}$
$l_{\text{Ni}}$	positive electrode thickness, $\text{cm}$
$l_{km}$	macroscopic diffusion length of species in phase $k$ , $\text{cm}$
$Q$	charge per unit projected area of the electrode, $\text{C}/\text{cm}^2$
$p$	reaction order of atomic hydrogen in the metal hydride electrode
$P$	cell pressure, $\text{atm}$
$P_i$	species partial pressure, $\text{atm}$
$R$	universal gas constant, $8.3143 \text{ J}/\text{mol} \cdot \text{K}$ or $82.06 \text{ atm} \cdot \text{cm}^3/\text{mol} \cdot \text{K}$
$R_{sb}$	area-specific electrical resistance across the solid/substrate interface, $\Omega \cdot \text{cm}^2$
$R_{se}$	area-specific electrical resistance across the solid/electrolyte interface, $\Omega \cdot \text{cm}^2$
$r$	radial coordinate, $\text{cm}$
$r_0$	radius of cylindrical substrate, $\text{cm}$
$r_s$	radius of active material particles, $\text{cm}$
$T$	absolute temperature of the cell system, $\text{K}$
$t$	time, $\text{s}$
$t_-^0$	transference number of $\text{OH}^-$ with respect to the solvent velocity
$U_{j,\text{ref}}$	open-circuit potential for reaction $j$ at the reference state with respect to a $\text{Hg}/\text{HgO}$ reference electrode, $\text{V}$
$x$	$x$ - coordinate, $\text{cm}$

### Greek symbol

$\alpha_{aj}, \alpha_{cj}$	anodic and cathodic transfer coefficients for reaction $j$
$\varepsilon$	volume fraction of a phase
$\eta_j$	surface overpotential of electrode reaction $j$ , $\text{V}$
$\theta$	interfacial state of charge of the nickel active material
$\kappa$	conductivity of an electrolyte, $\text{S}/\text{cm}$
$\kappa_D$	diffusional conductivity of a species, $\text{A}/\text{cm}$
$\rho_{\text{avg}}$	average density of active material, $\text{g}/\text{cm}^3$
$\sigma$	conductivity of the active solid material, $\text{S}/\text{cm}$
$\phi$	potential in a phase, $\text{V}$
$\bar{\phi}_{se}$	surface potential in the solid phase at the solid/electrolyte interface, $\text{V}$

### Subscript

$b$	substrate
-----	-----------

<i>e</i>	electrolyte phase
<i>eff</i>	effective
<i>eg</i>	electrolyte-gas interface
<i>g</i>	gas phase
MH	metal hydride active material
<i>max</i>	maximum value
<i>mix</i>	mixture
Ni	nickel active material
<i>ref</i>	with respect to a reference state
<i>s</i>	solid phase
<i>sb</i>	solid/substrate interface
<i>se</i>	solid/electrolyte interface
<i>o</i>	initial value

#### Superscript

<i>eff</i>	effective
H	species hydrogen or proton
H <sub>2</sub> O	solvent water
O <sub>2</sub>	oxygen
OH	species OH <sup>-</sup>

## INTRODUCTION

The nickel-metal hydride (Ni-MH) battery holds promise for application in electric and hybrid-electric vehicles because it has a high specific energy, high specific power, long cycle life, and most importantly no poisonous heavy metals [1]. Extensive efforts have been and continue to be made to develop advanced Ni-MH batteries to meet the stringent requirements of electric vehicle batteries [2, 3]. Mathematical modeling is indispensable in this process because a cell model, once validated experimentally, can be used to identify cell-limiting mechanisms and forecast the cell performance for design, scale-up, and optimization.

A Ni-MH cell is a dual-intercalation electrochemical system in which proton insertion in the positive solid nickel electrode and hydrogen de-insertion in the negative metal hydride electrode occurs during discharge, and vice versa during charge. Figure 1 schematically illustrates these processes. The open-circuit potentials of both electrodes are functions of the local state of charge [3, 4] therefore the cell behavior is strongly dependent on the utilization of active materials. In addition, discharge or charge of a Ni-MH cell is controlled by a number of factors, including the finite rate of solid state diffusion inside active material particles of either one or both electrodes, charge transfer kinetics at the electrode/electrolyte interface, and ohmic drop through the electrolyte phase. Any of these factors may result in too low a cell potential before the active materials loaded in the cell are completely used up. As a result, the inefficient utilization of active materials becomes a critical issue, particularly for electric and hybrid-electric vehicle batteries.

Operation of a sealed Ni-MH cell is also accompanied by oxygen reactions. Oxygen may be generated at the nickel electrode and cause an excessive build-up of pressure during charge and overcharge. This gassing strongly affects the performance and life of Ni-MH batteries as well as controls the charge acceptance at high charging rates. It also raises safety concerns in practical applications. A battery must be carefully designed so that the oxygen is effectively transported to and recombined at the metal hydride electrode, preventing the cell pressure from rising drastically. It is thus imperative to develop predictive capabilities for not only the active material utilization but also the cell conditions resulting from the oxygen reactions in advanced Ni-MH batteries.

Efforts have been made to model Ni-MH batteries based on the volume-averaging approach and the macro-homogeneous theory of Newman [5]. An excellent overview of the electrochemistry and transport phenomena occurring in the Ni-MH battery system was given by Fuller and Newman

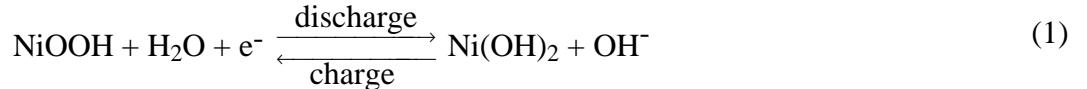
[3]. A mathematical model for the discharge of a Ni-MH cell was recently developed by Paxton and Newman [6]. Their analysis was restricted to the discharge behavior of the Ni-MH cell. The oxygen reactions, which are important during charge and overcharge [7], were excluded. On the other hand, the most recent model of Gu et al. [9] included the oxygen generation at the nickel electrode and recombination at the metal hydride electrode using a simplified two-phase approach. That is, the oxygen was treated as a neutral species dissolved in the liquid electrolyte. Extensive numerical studies have been carried out using this model to assess the effects of the electrode capacity ratio and charge/discharge rates [10]. A sensitivity analysis was also performed for various transport and thermodynamic properties such as the diffusion coefficient, transfer number, and exchange current density [10]. However, such an effective two-phase model cannot delineate many important effects of oxygen reactions, for example, those involving the charge acceptance, cell pressure, and self-discharge. Furthermore, both models of Paxton and Newman [6] and Gu et al. [9] have yet to be validated against experiments.

The purpose of the present work is therefore three-fold: (1) to extend the previous two-phase Ni-MH model [9] by incorporating an additional gas phase; (2) to provide experimental validation of the present Ni-MH cell model; and (3) to fully explore the effects of the oxygen evolution on the cell performance and operating conditions. In what follows, a three-phase mathematical model which considers the oxygen transport through both electrolyte and gas phases is presented for the Ni-MH cell based on the micro-macroscopic coupled model proposed by Wang et al. [8]. It will be shown that the present three-phase model essentially reduces to the previous two-phase model [9] provided chemical equilibrium exists in both electrolyte and gas phases and a mixture concentration of oxygen is employed to represent the total oxygen content in a control volume. A sealed Ni-MH cell is used to conduct discharge experiments. The test data along with other literature data [11] are then used to validate the present model. Finally, numerical simulations are carried out to address such issues as charge acceptance, cell pressure build-up during charge and overcharge, and self-discharge.

## MATHEMATICAL MODEL

The Ni-MH cell under consideration is composed of three regions: a negative electrode (metal hydride powders), a positive electrode (porous nickel oxyhydroxide), and a separator. The separator, located between electrodes, acts as an electronic insulator, as schematically shown in Fig. 1. A concentrated KOH aqueous solution serves as the electrolyte. Electrochemical reactions taking place at the electrode/electrolyte interface inside each electrode during discharge and charge are given by

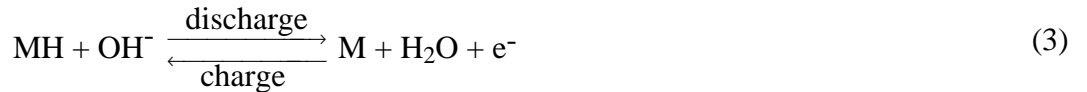
Positive electrode



with the side reaction



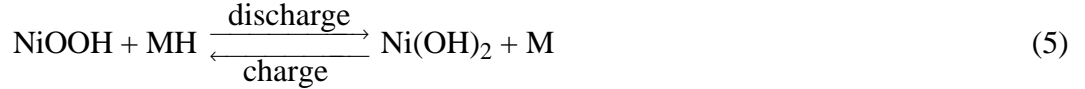
Negative electrode



with the side reaction



Combination of Eq. 1 with Eq. 3 yields the overall cell reaction



while side reactions (2) and (4) constitute the oxygen circulation inside the cell [12]. In the presence of oxygen reactions, a Ni-MH cell is a three-phase system consisting of the solid matrix, the liquid electrolyte, and a gas phase. During charging and overcharging, oxygen is generated at the nickel/electrolyte interface and may evolve into the gas phase after exceeding its solubility limit in the liquid electrolyte. The oxygen can then be transported, via the liquid and gas phases, from the nickel to MH electrode where the oxygen gas may dissolve in the electrolyte and be reduced at the MH/electrolyte interface. Such a process forms an internal oxygen cycle in a recombinant cell like the Ni-MH cell [12]. The accumulation of oxygen in the gas phase will lead to a cell pressure build-up.

### Assumptions

- (i) The nickel electrode consists of composite cylindrical needles with a substrate inside (see Fig.1) and its porosity remains constant;
- (ii) The MH electrode consists of spherical particles with uniform size and constant porosity;
- (iii) There is a continuous gas-pore network with a uniform and constant volume fraction in each region of the cell, and there also exists a gas reservoir above the cell with a constant volume. The ideal gas law applies;
- (iv) The solid phase is completely wetted by the electrolyte. In other words, there is no contact between solid active material and the gas phase;
- (v) Convection effects in the electrolyte and gas are neglected, leaving the species transport to diffusion and/or migration;
- (vi) Interfacial chemical equilibrium exists in the liquid phase for all species other than the dissolved oxygen, which has a relatively small value of mass diffusivity in the liquid electrolyte. Electrical equilibrium exists in the liquid phase due to the large value of ionic conductivity of the electrolyte; and finally
- (vii) Thermal effects are ignored.

With the above assumptions, a one-dimensional model for the three-phase electrochemical system can be extracted from the previously developed micro-macroscopic coupled model [8], as demonstrated below. Note that the volume-averaging symbol has been dropped here for convenience. For a species existing only in one phase, the corresponding subscript has also been dropped for simplicity.

### Governing equations

*Reaction rates.*— Reaction rates for the various charge-transfer reactions involved in a Ni-MH cell can be derived from the general Butler-Volmer equation with respect to a specified reference state. Following De Vidts and White [13] and De Vidts et al. [14], we have

$$\bar{i}_{n1} = i_{o1,\text{ref}} \left[ \left( \frac{c_{\text{OH}}}{c_{\text{ref}}} \right) \left( \frac{\bar{c}_{\text{H}}}{c_{\text{ref}}} \right) \exp\left( \frac{\alpha_{a1}F}{RT} \eta_1 \right) - \left( \frac{c_{\text{max}}^{\text{H}} - \bar{c}_{\text{H}}}{c_{\text{max}}^{\text{H}} - c_{\text{ref}}^{\text{H}}} \right) \exp\left( -\frac{\alpha_{c1}F}{RT} \eta_1 \right) \right] \quad (6)$$

$$\bar{i}_{n2} = i_{o2,\text{ref}} \left[ \left( \frac{c_{\text{OH}}}{c_{\text{ref}}} \right)^2 \exp\left( \frac{\alpha_{a2}F}{RT} \eta_2 \right) - \left( \frac{c_{\text{O}_2}}{c_{\text{ref}}} \right) \exp\left( -\frac{\alpha_{c2}F}{RT} \eta_2 \right) \right] \quad (7)$$

$$\bar{i}_{n3} = i_{o3,\text{ref}} \left[ \left( \frac{c_{\text{OH}}}{c_{\text{ref}}} \right) \left( \frac{\bar{c}_{\text{H}}}{c_{\text{ref}}} \right)^p \exp\left( \frac{\alpha_{a3}F}{RT} \eta_3 \right) - \exp\left( -\frac{\alpha_{c3}F}{RT} \eta_3 \right) \right] \quad (8)$$

$$\bar{i}_{n4} = i_{o4,ref} \left[ \left( \frac{c_{OH}^{OH}}{c_{ref}^{OH}} \right)^2 \exp\left( \frac{\alpha_a 4F}{RT} \eta_4 \right) - \left( \frac{c_{O_2}^{O_2}}{c_{ref}^{O_2}} \right) \exp\left( -\frac{\alpha_c 4F}{RT} \eta_4 \right) \right] \quad (9)$$

for various reactions, with  $j = 1, 2, 3,$  and  $4$  referring to reactions (1), (2), (3), and (4), respectively. In the above  $c$ 's with various superscripts stand for their concentrations and  $\eta_j$  is the surface overpotential of reaction  $j$ , i.e.

$$\eta_j = \bar{\Phi}_{se} - \phi_e - U_{j,ref} \quad j=1, 2, 3, \text{ and } 4 \quad (10)$$

where  $U_{j,ref}$  stands for the open-circuit (i.e. equilibrium) potential of reaction  $j$  at the reference state with respect to a Hg/HgO reference electrode. In the present work, we have

$$U_{1,ref} = 0.427 + \frac{RT}{F} k(2\theta - 1) \quad (11)$$

with

$$\theta = 1 - \frac{\bar{c}^H}{c_{max}^H} \quad (12)$$

for reaction (1) [4,13],

$$U_{3,ref} = -0.9263 - \frac{RT}{F} \ln(c_{ref}^H)^p \quad (13)$$

for reaction (3) [14], and

$$U_{2,ref} = U_{4,ref} = 0.3027 \quad (14)$$

for oxygen generation and recombination reactions (2) and (4) [4, 13].

In Eq. 11,  $\theta$  is the interfacial state of charge of the nickel active material as defined by Eq. 12, and  $k$  is the intercalation constant which accounts for the interactions between the species in a solid solution [15, 16]. In other words, the second term on the right side of Eq. 11 is used to account for the deviation of the equilibrium potential of the nickel electrode from the ideal solid solution behavior. Positive and negative values of  $k$  reflect the positive and negative deviations from the ideal, respectively. The shape of discharge curves of a Ni-based cell could be strongly affected by the value of  $k$  [4, 17]. An appropriate value of the intercalation constant taken from Ref. 16 is used in the present work, as listed in Table II.

In Eqs. 8 and 13 the index  $p$  is the reaction order of atomic hydrogen in the MH electrode. Its value varies with different types of metal hydride active materials. For AB<sub>5</sub>-type metal hydrides like LaNi<sub>5</sub>, a value of 1/6 may be chosen if we assume that the order of reaction corresponds to the stoichiometric coefficients of the reaction [4, 14].

*Species conservation equations.*—There are two species in the liquid electrolyte that participate in charge-transfer reactions under consideration: an ionic species OH<sup>-</sup> and a neutral species O<sub>2</sub>. The gas phase is composed of gaseous O<sub>2</sub>, water vapor, and other inert species (*e.g.* nitrogen). Under the foregoing assumptions, the convection term vanishes and there is no movement of electrolyte/electrode interface due to a constant porosity of the electrode. Applying the general volume-averaged conservation equation of species (i.e., Eq. 41 in Ref. 8) and making use of the interfacial balance condition (i.e., Eq. 49 in Ref. 8) to species OH<sup>-</sup> and O<sub>2</sub>, respectively, yield

$$\frac{\partial(\epsilon_e c_e^{OH})}{\partial t} = \nabla \cdot (D_{eff}^{OH} \nabla c_e^{OH}) + \frac{t_-^0 - 1}{F} j^{OH} \quad (15)$$

$$\frac{\partial(\epsilon_e c_e^{O_2})}{\partial t} = \nabla \cdot (D_{e,eff}^{O_2} \nabla c_e^{O_2}) + \frac{1}{4F} j^{O_2} + J_{eg}^{O_2} \quad (16)$$

$$\frac{\partial(\epsilon_g c_g^{O_2})}{\partial t} = \nabla \cdot (D_{g,eff}^{O_2} \nabla c_g^{O_2}) - J_{eg}^{O_2} \quad (17)$$

Here,  $t_-^0$  is the transference number of the OH<sup>-</sup> with respect to the velocity of the solvent and  $D_{eff}^{OH}$  is an effective diffusion coefficient including the effect of tortuosity, i.e.

$$D_{\text{eff}}^{\text{OH}} = D^{\text{OH}} \epsilon_e^{1.5} \quad (18)$$

where  $D^{\text{OH}}$  is the mass diffusion coefficient of species OH<sup>-</sup> in the electrolyte KOH. Likewise, the effective mass diffusivity of oxygen in Eqs. 16 and 17 follows the same Bruggeman relation as given in Eq. 18.

The last term in Eq. 15 is proportional to  $j^{\text{OH}}$ , the total transfer current from all electrochemical reactions that generate or consume the species OH<sup>-</sup> at the electrode/electrolyte interface, namely

$$j^{\text{OH}} = \begin{cases} a_{\text{Ni}}(\bar{i}_{n1} + \bar{i}_{n2}) & \text{in the nickel electrode} \\ 0 & \text{in the separator} \\ a_{\text{MH}}(\bar{i}_{n3} + \bar{i}_{n4}) & \text{in the MH electrode} \end{cases} \quad (19)$$

Similarly,  $j^{\text{O}_2}$  is the transfer current associated with the generation or consumption of oxygen, i.e.

$$j^{\text{O}_2} = \begin{cases} a_{\text{Ni}}\bar{i}_{n2} & \text{in the nickel electrode} \\ 0 & \text{in the separator} \\ a_{\text{MH}}\bar{i}_{n4} & \text{in the MH electrode} \end{cases} \quad (20)$$

In Eqs. 16 and 17  $J_{eg}^{\text{O}_2}$  is the interfacial mass transfer rate of oxygen from the gas to the liquid phase as expressed by Eq. 42 in Ref. 8. Assuming that oxygen absorption/desorption takes place in the diffusion mode (i.e., the nucleation does not occur) [18], it follows that

$$J_{eg}^{\text{O}_2} = K(\bar{c}_e^{\text{O}_2} - c_e^{\text{O}_2}) \quad (21)$$

where  $K$  is the interfacial mass transfer coefficient on the liquid side. The difference between the phase-averaged concentration,  $c_e^{\text{O}_2}$ , and the interfacial concentration of oxygen,  $\bar{c}_e^{\text{O}_2}$ , provides a driving force for the interfacial mass transfer from the liquid to the gas phase. Using the concept of diffusion length proposed in Ref. 8, the mass transfer coefficient can further be expressed as

$$K = a_{eg} \frac{D_e^{\text{O}_2}}{l_{eg}} \quad (22)$$

where  $l_{eg}$  is a microscopic diffusion length whose expression has been derived by Wang et al. [8].

There exists, however, the interfacial chemical equilibrium in the gas phase due to the large value of oxygen mass-diffusivity in gases. Indeed, mass transfer in an absorption/desorption process of a rarely soluble gas (e.g. O<sub>2</sub> in the liquid water) is controlled by the liquid-side resistance [18]. Thus

$$\bar{c}_g^{\text{O}_2} = c_g^{\text{O}_2} \quad (23)$$

In addition, Henry's law applies to the liquid/gas interface due to the low solubility of oxygen in the KOH solution, i.e.

$$\bar{c}_e^{\text{O}_2} = H' \bar{c}_g^{\text{O}_2} = H' c_g^{\text{O}_2} = H P^{\text{O}_2} \quad (24)$$

where  $H$  (or  $H'$ ) is the Henry constant for the O<sub>2</sub>-KOH aqueous solution system and its value is listed in Table II.  $H'$  can be related to  $H$  via the ideal gas law (i.e.,  $H'/RT$ ). Equation 24 relates  $\bar{c}_e^{\text{O}_2}$  to  $c_g^{\text{O}_2}$  (or  $P^{\text{O}_2}$ ), thus rendering Eqs. 16 and 17 for two independent unknowns:  $c_e^{\text{O}_2}$  and  $c_g^{\text{O}_2}$ .

A simplification of Eq. 17 is possible because oxygen diffusion across the cell in the gas phase is inherently faster than that in the liquid phase due to the much larger diffusion coefficient of oxygen in gases [12]. Furthermore, oxygen transport is facilitated by the presence of a gas reservoir above the cell. Hence, the gas is relatively well mixed across a thin cell and it is safe to assume that the gaseous oxygen concentration is uniform throughout the cell [19, 20]. Integrating Eq. 17 over the entire cell then gives

$$\frac{\partial(c_g^{O_2})}{\partial t} = -\frac{1}{V_g} \int_V J_{eg}^{O_2} dV \quad (25)$$

This equation in place of Eq. 17 is used in all simulations to be reported in the present paper.

In addition to the OH<sup>-</sup> in the liquid phase and O<sub>2</sub> in both liquid and gas phases, one species, either proton or atomic hydrogen, is present in the solid phase of the nickel and MH electrodes, respectively. Represented by a uniform symbol H, the conservation equation of either proton or hydrogen is given by [9]

$$\frac{\partial(\epsilon_s c^H)}{\partial t} = \frac{j^H}{F} \quad (26)$$

where

$$j^H = \begin{cases} a_{Ni} \bar{i}_{n1} & \text{in the nickel electrode} \\ 0 & \text{in the separator} \\ a_{MH} \bar{i}_{n3} & \text{in the MH electrode} \end{cases} \quad (27)$$

The interfacial balance of H in either nickel or MH electrode becomes [9]

$$\frac{D^H}{l_{se}} (\bar{c}_{se}^H - c^H) = \frac{j^H}{a_{se} F} \quad (28)$$

where  $\bar{c}_{se}^H$  is the proton or hydrogen concentration at the electrode/electrolyte interface and  $l_{se}$  is the diffusion length expressed as [8]

$$l_{se} = \frac{r_s + r_o}{4} - \frac{r_s r_o}{3(r_s - r_o)} + \frac{2r_o^3}{3(r_s^2 - r_o^2)} \quad (29)$$

for the cylindrical morphology of the nickel electrode and

$$l_{se} = \frac{r_s}{5} \quad (30)$$

for the spherical morphology of the MH electrode.

Before leaving this subsection, a particular case for Eqs. 16 and 17 in the limit of interfacial chemical equilibrium of oxygen in the liquid electrolyte (i.e.,  $c_e^{O_2} = \bar{c}_e^{O_2}$ ) is worth exploring. In this case,  $c_e^{O_2} = \bar{c}_e^{O_2} = H' c_g^{O_2}$  according to Eq. 24. It follows that Eqs. 16 and 17 can be combined into a single equation in terms of a mixture concentration of oxygen over a control volume; namely

$$c_{mix}^{O_2} = c_e^{O_2} + \left( \frac{\epsilon_g}{\epsilon_e} \right) c_g^{O_2} \quad (31)$$

Adding up Eqs. 16 and 17 and canceling the interfacial mass transfer term yield

$$\frac{\partial(\epsilon_e c_{mix}^{O_2})}{\partial t} = \nabla \cdot (D_{eff}^{O_2} \nabla c_{mix}^{O_2}) + \frac{1}{4F} j^{O_2} \quad (32)$$

where

$$D_{\text{eff}}^{\text{O}_2} = \frac{H'D_{e,\text{eff}}^{\text{O}_2} + D_{g,\text{eff}}^{\text{O}_2}}{H' + \frac{\epsilon_g}{\epsilon_e}} \approx \epsilon_e \epsilon_g^{0.5} D_g^{\text{O}_2} \quad (33)$$

In arriving at the last equality of Eq. 33, the Bruggeman relation as given by Eq. 18 for the effective mass diffusivity of gaseous oxygen is used and the Henry constant is assumed to be very small ( $\sim 10^{-12}$ ). Equation 32 is identical to the species conservation equation in Gu's model [9] provided Eq. 33 is used to estimate the effective mass diffusivity of oxygen. In other words, all previous two-phase models [4, 21] are mathematically equivalent to the present three-phase model under the assumption of local equilibrium of oxygen in both electrolyte and gas phases. Equation 33 then provides a rigorous means to estimate the mass diffusivity of oxygen in this case. It should be reiterated that Eqs. 32 and 33 are derived based on the equilibrium assumption and are not valid in high-rate charging and overcharging situations.

*Charge conservation equations.*—For the liquid phase, the charge conservation equation takes the following form [9]

$$\nabla \cdot (\kappa^{\text{eff}} \nabla \phi_e) + \nabla \cdot (\kappa_{\text{D}}^{\text{eff}} \nabla \ln c^{\text{OH}}) + j^{\text{OH}} = 0 \quad (34)$$

This equation can be used to determine the electrical potential in the electrolyte phase,  $\phi_e$ . Here, the effective ionic conductivity is given by  $\kappa^{\text{eff}} = \epsilon_e^{1.5} \kappa$  following Eq. 18, while  $\kappa_{\text{D}}^{\text{eff}}$  is the diffusional conductivity given by [8]

$$\kappa_{\text{D}}^{\text{eff}} = \frac{2RT\kappa^{\text{eff}}}{F} \left( 1 + \frac{d \ln f_{\pm}}{d \ln c^{\text{OH}}} \right) \left( 1 - t_-^{\circ} + \frac{c^{\text{OH}}}{2c_{\text{H}_2\text{O}}} \right) \quad (35)$$

The transfer current in Eq. 34,  $j^{\text{OH}}$ , is the same as given in Eq. 19.

For the solid phase, the charge conservation equation is expressed as [9]

$$\nabla \cdot (\sigma^{\text{eff}} \nabla \phi_s) - j^{\text{OH}} + a_{sb} \frac{\bar{\phi}_{sb} - \phi_s}{R_{sb}} = 0 \quad (36)$$

where the second term represents the transfer current generated at the electrode/electrolyte interface, and the third term stands for the current conducted into a substrate, with  $a_{sb}$  and  $\bar{\phi}_{sb}$  representing the specific area and potential at the active material/substrate interface, respectively. This term is absent on the MH electrode and is relevant only to the nickel electrode where a substrate is embedded in the solid material to improve the electronic conductivity. In this case, the substrate potential  $\bar{\phi}_{sb}$  usually remains constant due to a large value of the electronic conductivity.

In addition to the two volume-averaged conservation equations for charge, the interfacial charge balance at the electrode/electrolyte interface gives [9]

$$\frac{\bar{\phi}_{se} - \phi_s}{R_{se}} = - \frac{j^{\text{OH}}}{a_{se}} \quad (37)$$

where  $\bar{\phi}_{se}$  is the solid potential at the interface and is needed to calculate the interfacial overpotential  $\eta$ ; see Eq. 10. The area-specific electrical resistances appearing in Eqs. 36 and 37 are directly proportional to the particle size of the active material and inversely proportional to the electronic conductivity. For the MH electrode, the respective electronic conductivity is sufficiently high, therefore the electric resistance  $R_{se}$  approaches zero, and Eq. 37 essentially reduces to

$$\bar{\phi}_{se} = \phi_s \quad (38)$$

That is, electrical equilibrium exists in the MH electrode. In contrast, the nickel electrode in the semiconducting state has a relatively low electronic conductivity so that the electrical equilibrium assumption does not hold true. In this case, the microscopic area-specific electrical resistances derived by Wang et al. [8] can be used, i.e.

$$R_{sb} = \frac{r_0}{12} \left( \frac{r_s - r_0}{r_s + r_0} \right) \left( \frac{5r_s + 3r_0}{\sigma_0 r_0} + \frac{3r_s + r_0}{\sigma_s r_s} \right) \quad (39)$$

and

$$R_{se} = \frac{r_s}{12} \left( \frac{r_s - r_o}{r_s + r_o} \right) \left( \frac{r_s + 3r_o}{\sigma_o r_o} + \frac{3r_s + 5r_o}{\sigma_s r_s} \right) \quad (40)$$

where  $\sigma_o$  and  $\sigma_s$  denote the conductivities of the nickel active materials at the electrode/substrate and electrode/electrolyte interfaces, respectively.

The effective conductivity of the solid phase in Eq. 24,  $\sigma^{\text{eff}}$ , is related to the conductivity of the active materials,  $\sigma$ , by [13, 14]

$$\sigma^{\text{eff}} = \varepsilon_s \sigma \quad (41)$$

where subscript  $s$  denotes either nickel or MH electrode. The conductivity of the nickel active material is a strong function of local state of charge [22], i.e.

$$\sigma = 0.1185 \exp \left[ -8.459 \left( \frac{c^{\text{H}}}{c_{\text{max}}^{\text{H}}} \right)^4 \right] \quad (42)$$

while the conductivity of the MH alloy is assumed to be at the value of 41505.1 S/cm [14]. The effective conductivity of the MH electrode is thus sufficiently high, leading to a virtually uniform potential distribution across the electrode.

In summary, a total of six governing equations, Eqs. 15, 16, 25, 26, 34, and 36, can be solved for the six unknowns:  $c^{\text{OH}}$ ,  $c_e^{\text{O}_2}$ ,  $c_g^{\text{O}_2}$ ,  $c^{\text{H}}$ ,  $\phi_e$ , and  $\phi_s$ . In addition, two interfacial balances,

Eqs. 28, and 37, are provided to determine two interfacial quantities:  $\bar{c}_{se}^{\text{H}}$  and  $\bar{\phi}_{se}$ .

*Initial /boundary conditions.*—Uniform initial conditions are assumed, i.e.

$$c^{\text{OH}} = c_o^{\text{OH}}, c_e^{\text{O}_2} = \text{HP}_o^{\text{O}_2}, c_g^{\text{O}_2} = \frac{\text{P}_o^{\text{O}_2}}{\text{RT}}, \text{ and } c^{\text{H}} = c_o^{\text{H}} \quad (43)$$

Boundary conditions at the positive electrode/current collector boundary ( $x=L$ ) include

$$\frac{\partial c^{\text{OH}}}{\partial x} = 0, \frac{\partial c_e^{\text{O}_2}}{\partial x} = 0, \frac{\partial c^{\text{H}}}{\partial x} = 0, \frac{\partial \phi_e}{\partial x} = 0, \text{ and } \phi_s = \bar{\phi}_{sb} \quad (44)$$

At the negative electrode ( $x=0$ ), there is no flux of species and all current goes through the solid phase

$$\frac{\partial c^{\text{OH}}}{\partial x} = 0, \frac{\partial c_e^{\text{O}_2}}{\partial x} = 0, \frac{\partial c^{\text{H}}}{\partial x} = 0, \frac{\partial \phi_e}{\partial x} = 0, \text{ and } -\sigma^{\text{eff}} \frac{\partial \phi_s}{\partial x} = I \quad (45)$$

### Numerical Procedures

The equations in the micro-macroscopic model presented above were discretized using a finite volume method [23] and solved using a general-purpose computational fluid dynamic (CFD) code. Details have been given in the previous works [24, 25]. It should be mentioned that stringent numerical tests were performed to ensure that the solutions were independent of the grid size and time step. It was found that the typical number of grid lines across the cell width is about 60 (i.e., the size of a finite volume is about 1/20 of an electrode thickness) and the time step normally ranges from 10 to 30 seconds, except for the end of discharge when smaller time steps were required. The equations were solved as a simultaneous set, and convergence was considered to be met when the relative error in each field between two consecutive iterations was less than  $10^{-5}$ . A typical transient simulation for one dimensional problems required no more than 10 minutes of CPU time on an HP B160L workstation (160 MHz CPU, SPECfp95 7.39).

### Cell Parameters

Important cell parameters to be discussed in the Results and Discussion section are defined below.

*State of charge and depth of discharge.*—The state of charge (SOC) is defined as

$$\text{SOC} = \frac{\int_0^t \int_0^{l_{\text{Ni}}} a_{\text{Ni}} i_{\text{n1}} dx dt}{Q_{\text{max}}} \quad (46)$$

for charge processes and the depth of discharge (DOD) is then defined as

$$\text{DOD} = 1 + \frac{\int_0^t \int_0^{l_{\text{Ni}}} a_{\text{Ni}} i_{\text{n1}} dx dt}{Q_{\text{max}}} \quad (47)$$

for discharge processes. In Eqs. 46 and 47  $t$  is the time elapsed from a full discharge or charge state.  $Q_{\text{max}}$  is the maximum theoretical charge capacity of the nickel electrode per unit of the projected electrode area, because Ni-MH cells are generally designed to be positive electrode-limiting to avoid hydrogen evolution in the negative electrode when fully charged and overcharged.

*Charge acceptance.*—The charge acceptance of a cell is defined as the ratio of partial charge used by the electrochemical reaction to reverse the active materials to the total charge applied to the cell [12], i.e.

$$\text{Charge acceptance} = \frac{\int_0^t \int_0^{l_{\text{Ni}}} a_{\text{Ni}} i_{\text{n1}} dx dt}{\int_0^t I dt} \quad (48)$$

Clearly, the charge acceptance is a function of time or the cell SOC, and can be thought of as the instantaneous charge efficiency.

*Cell pressure.*—In a sealed Ni-MH cell, the cell pressure results from the overall balance of oxygen generation, transport, and recombination [12]. The cell pressure increases whenever the oxygen generation rate is higher than its recombination rate, which usually occurs during high rate charge and overcharge. The increase in the oxygen concentration in the gas phase directly contributes to the cell pressure build-up. The cell pressure is calculated from the ideal gas law:

$$P = P_0 + (P^{\text{O}_2} - P_0^{\text{O}_2}) = P_0 + (c_g^{\text{O}_2} - c_{g,0}^{\text{O}_2})RT \quad (49)$$

where  $P_0$  is the initial (reference) cell pressure and is set to be zero in the present work.

## EXPERIMENTAL

A hydrogen storage alloy of AB<sub>5</sub>-based alloy was prepared by induction melting and rapid cooling. The cast alloy was annealed at 900 °C for 10 hours in vacuum. The cast alloy was then mechanically pulverized to obtain a sifted particle size ranging between 40 μm to 50 μm.

For the specific capacity measurements, the alloy powders were mixed with nickel powder in a weight ratio of 1:3 together and a small amount of polyvinyl alcohol (PVA) solution was used as the binder. The powders of solution were pressed at a pressure of 150 kg/cm<sup>2</sup> after vacuum drying at 150 °C. A sintered nickel hydroxide (Ni(OH)<sub>2</sub>/NiOOH) plate and Hg/HgO 6M KOH electrode were used as counter and reference electrodes, respectively. The charge and discharge current was 100 mA/g. The end of discharge was set to -0.5 V vs. Hg/HgO. The MH alloy powders with a maximum specific capacity of 281 mAh/g at the 100 mA/g discharge current were used as the active materials of the negative electrode.

The composition of the negative electrode in our experiments was 100 g Ni-coated MH alloy powder, 10 g nickel powder, and 3wt.% polytetrafluoroethylene (PTFE) dispersion (60%). The weight percentage of the MH alloy powder in the negative electrode was 68-70%. The mixture of MH alloy powders, nickel powders, and PTFE dispersion was coated onto two sides of a porous nickel plate (0.04-0.05mm in thickness), and roller pressed in order to obtain a sheet. A sintered

nickel hydroxide ( $\text{Ni(OH)}_2/\text{NiOOH}$ ) plate was used as the positive electrode of the Ni/MH battery. The content of the active material,  $\text{Ni(OH)}_2/\text{NiOOH}$ , was about 65% of the weight of the positive electrode. The dimensions of the negative and positive plates were  $95 \times 40 \times 0.40 \text{ mm}^2$  and  $75 \times 40 \times 0.7 \text{ mm}^2$ , respectively, with the respective maximum capacities of 1.6 Ah/g and 1.0 Ah/g. The thickness of the separator (polyamide non-woven cloth) was 0.1mm. The electrolyte in the Ni/MH battery was a 7M KOH-1M LiOH aqueous solution. The sealed cell (AA size, 1 Ah capacity) was constructed by rolling together the MH electrode plate, separator and sintered nickel plate. The cell was charged at 1 A current for 1.1-1.2 h and discharged at 0.5-3 A current to 1 V.

## RESULTS AND DISCUSSION

### *Code validation*

Comparisons are made between experimental and predicted data to validate the numerical model developed in the previous section. The measured discharge data as described in the preceding section along with a set of experimental data available in the literature [11] are used in this work. Their cell-specific parameters are summarized in Table I, respectively. Cell 1 refers to the present experimental study, while cell 2 was used in the experiments of Sakai et al. [11]. Both cells are positive electrode-limiting so as to avoid hydrogen generation in the negative electrode when charging or overcharging a cell. Due to a lack of detailed information about cell 2, its geometric data such as electrode thicknesses are estimated from the given capacities. Parameters used in numerical simulations are listed in Table II. Some of parameters are related to one another and equations for their conversions can be found in Ref. 13. The transport and thermodynamic properties of the electrolyte are calculated via expressions correlated by De Vidts and White [13].

Figure 2 shows the comparison of predicted cell potentials with experimental results for cell 1. The applied discharge currents are 0.5A, 1.0A, and 1.5A, corresponding to the discharge rates of C/2, C/1, and 1.5C, respectively. The simulated cell potential curves agree well with the experimental data, especially with respect to the discharge capacity and midpoint cell potential. The cell potential decreases gradually with time due to the decrease of the hydrogen concentration in the metal hydride and the increase of the proton concentration in the nickel active material. The experimental discharge curves exhibit the following characteristics: an initial quick drop in the cell potential, followed by a large portion of a much more shallow potential drop whose slope depends on the discharge rate, and ended with a drastic drop in the cell potential due to the depletion of active materials in the nickel electrode (positive electrode-limiting). The rate of discharge largely affects the cell behavior; the larger the rate is, the more quickly the cell potential drops. The predicted discharge curves are flatter than the experimental ones during the very initial stage of discharge. This may be attributed to the occurrence of phases other than the conventional  $\beta$ -NiOOH, such as  $\gamma$ -NiOOH, during extensive cycling and/or overcharge; and it should be possible to incorporate a multiple-phase reaction mechanism in the present model to reduce such discrepancies and hence improve the accuracy of the predictions [17].

Figure 3(a) shows a comparison of predicted and measured cell discharge potentials for cell 2. Good agreement was achieved again. The applied discharge currents were 10A, 50A, and 100A, corresponding to the discharge rates of C/3, 1.7C, and 3.3C, respectively. The same trend in the cell potential as for cell 1 can be observed. The initial quick drop in the cell potential, however, is not as large as that of cell 1 (see Fig. 2), indicating that the above-mentioned phase occurrence may depend on electrode materials and/or the electrode age.

Figure 3(b) displays a comparison of predicted and measured cell charge potentials for cell 2 with good agreement. It can be seen that the general shape of the experimental charge curves were successfully captured by the model. The charge currents are 10A, 30A, and 60A, corresponding to the charge rates of C/3, C/1, and 2C, respectively. Each charge experiment continued until the 100% charge input was achieved. That is, the cell was charged 3 hours, 1 hour, and 0.5 hour, respectively. During charge, the cell potential exhibits a quick rise at the beginning of charge, followed by a stage of gradually increasing potential. The larger the charge rate is, the more

quickly the cell potential increases. The actual state of charge, however, did not always reach 100%. For example, it was reported that the coulombic efficiency is 94% when the cell is charged at 2C rate [11]. From the predicted charge curve for 60 A, it can be observed that the increase in the cell potential becomes slower and experiences a peak close to 100% charge input. This is because the oxygen reactions become significant at this point and the cell potential is virtually a mixed potential of both primary and oxygen reactions [12].

#### *Effect of oxygen reactions during charge*

Oxygen is generated at the nickel electrode (Eq. 2) and recombined at the MH electrode (Eq. 4) during charge and overcharge. The rates of the oxygen generation and recombination are controlled by the exchange current densities appearing in their respective kinetics equations (Eqs. 7 and 9). The exchange current density for the oxygen generation is dependent on the surface conditions of the nickel oxide, with an order of  $10^{-11}$  A/cm<sup>2</sup> corresponding to a surface of minimum roughness [26]. A parametric study was done in the present work to examine the order of magnitude of the exchange current density for the oxygen generation at the nickel electrode in the Ni-MH cell of interest.

The exchange current density for oxygen recombination at the MH electrode may also be surface condition-dependent. However, the rate of oxygen recombination at the MH electrode is normally fast enough that the oxygen reduction is limited by the oxygen transport from the nickel to MH electrode [12]. An exchange current density of the order of  $10^{-11}$  A/cm<sup>2</sup> is high enough to recombine all oxygen reaching the MH electrode and is used in the present work to describe the oxygen recombination at the MH electrode.

Numerical simulations for cell 2 are carried out to explore the effects of oxygen reactions on the cell performance during charge and overcharge. Figure 4 shows the cell state of charge during 2C charge as a result of oxygen reactions. It is clearly shown that the cell SOC decreases with the increase in the exchange current density or the oxygen generation rate, because a smaller portion of the current is actually used to charge the active materials. Without oxygen evolution, all charge input into the cell is used to reverse the active materials to the charged state and 100% SOC is expected at the end of 100% charge input. With oxygen reactions, part of input charge is consumed to generate oxygen rather than charge the active materials, thus reducing the charge efficiency. A drop in the SOC as big as 12% occurs when the exchange current density of oxygen generation is as large as  $10^{-10}$  A/cm<sup>2</sup>. Corresponding to the exchange current density of  $10^{-11}$  A/cm<sup>2</sup>, the cell SOC is predicted to be 93% at 100% charge input, a value very close to the measured value (94%) [11], indicating that this magnitude of the exchange current density may be realistic for the oxygen generation.

The fact that the actual state of charge is not equal to the charge input in the presence of oxygen reactions also effects on experimental measurements of electrochemical properties, such as the open-circuit potential, as functions of the state of charge. In other words, the state of charge can no longer be determined by simply measuring the charge input but needs to be estimated from e.g. Fig. 4 when the oxygen reactions are taken into account.

Figure 5 shows that the cell charge potential is strongly influenced by the oxygen generation rate. Without oxygen reactions, the cell potential keeps increasing to a preset cutoff potential, while with oxygen reactions the cell potential reaches a maximum and then gradually decreases due to the lower equilibrium potential of the oxygen reactions. The value of the maximum cell potential depends on the rate of the oxygen generation; it decreases as the oxygen generation rate increases. This information shown in Fig. 5(a) can be used to infer the magnitude of the exchange current density for the oxygen generation using a potential measurement in the range towards the end of charge and overcharge. The cell potential versus SOC is plotted in Fig. 5(b) for the various oxygen generation rates, showing that the cell potential peak becomes more pronounced with a smaller oxygen generation rate.

Figure 6 displays the effect of different exchange current densities for the oxygen generation reaction on the cell pressure. The larger the exchange current density, the earlier a build-up in cell pressure is witnessed. Signified by the cell pressure, significant oxygen generation occurs at as

low as 50% charge input for the exchange current density of  $10^{-10}$  A/cm<sup>2</sup>, while it occurs at 80% charge input as the exchange current density lowers to  $10^{-12}$  A/cm<sup>2</sup>. However, the cell pressure increases more quickly at a smaller exchange current density because a smaller amount of active materials is left to be charged. As a result, the oxygen generation is more significant. During overcharge, the increase in the cell pressure becomes slower and gradually approaches an equilibrium state where the oxygen generation and recombination rates become equal. This equilibrium state comes earlier as the exchange current density decreases. Consistent with the experimental observation [7], this unique behavior of the cell pressure can also be used to infer the value of the exchange current density for the oxygen generation from a pressure measurement.

The effects of the oxygen reactions on the cell behavior at various charging rates are shown in Fig. 7, where the exchange current density of the oxygen generation is fixed at  $10^{-11}$  A/cm<sup>2</sup>. Figure 7(a) shows that the cell SOC decreases with the charge rate when the charge input is constant, meaning that the charge efficiency decreases with the charge rate. At small charge rates, such as C/3 and C/1, the cell SOC can approach close to 100% with the 100% charge input, while it is only 93% at 2C rate and 84% at 6C rate. To achieve full charge, the cell usually has to be overcharged to the extent which not only depends on the charging rate but also the active materials making up the cell [12]. The predicted results shown in Fig. 7(a) are consistent with the recent experimental observations [7]. Figure 7(b) shows the cell potentials at various charging rates. All potential curves exhibit a similar trend: a quick jump in the cell potential at the very beginning of charge, followed by a gradual increase until reaching the peak potential, and finally a gradual decrease. However, the appearance of the potential peak at each charge rate is different. While distinctive potential peaks can be seen at large rates, the potential peak is virtually indiscernible at the rate as low as C/3, resulting in difficulties determining the end of charge for Ni-MH batteries via the time-dependent potential gradient method [28].

Figure 8 shows the charge acceptance versus SOC. It is obvious that the charge acceptance is strongly dependent on the cell SOC. When the cell SOC exceeds 80%, oxygen starts to evolve significantly at charge rates as low as C/3. In practice, it is always desired to charge a battery as quickly as possible. From Fig. 8, however, one can conclude that charging a cell at a constant high rate is impractical, because high-rate charging leads to a high rate of oxygen generation. It is worth noting that negligible oxygen evolution takes place at a rate as high as 10C when the cell SOC is below 20%. One can take this advantage and charge a Ni-MH battery at very high rate during the early stage of charge and gradually reduce the charge rate with increasing SOC to avoid the high rate of oxygen generation and maintain the highest charge efficiency throughout the charge process.

Figure 9 plots the cell pressure profiles at various charging rates. It is assumed in this work that the oxygen evolving into the gas phase is the only contributor to the cell pressure build-up. Hydrogen evolution may also contribute to the cell pressure increase. However, Ni-MH batteries are usually designed to be positive electrode-limiting and an excessive portion of the MH active materials at the discharged state is provided as a charge reserve to absorb hydrogen [12], so the hydrogen evolving into the gas phase can be neglected unless this charge reserve has been completely used up. It can be seen from Fig. 9 that the cell pressure increases substantially only after a certain point where the rate of oxygen generation at the nickel electrode begins to exceed the rate of oxygen recombination at the MH electrode. This onset of pressure build-up occurs earlier if the charge rate is higher. These predicted trends are in good agreement with the recent experiments [7]. A high pressure build-up inside the cell will present a safety concern. One way to reduce the cell pressure is to improve the internal oxygen circulation controlled by generation, transport, and recombination [12] and use proper charging algorithms [28].

The cell pressure build-up is strongly dependent on the value of the interfacial mass transfer coefficient for oxygen, as can be seen in Fig. 10. The cell pressure at the equilibrium state doubles as the interfacial mass transfer coefficient halves. The value of the interfacial mass transfer coefficient was chosen in the present work to make the predicted cell pressure reasonable. In practice, it should be determined experimentally.

### *Effect of oxygen evolution during discharge*

Numerical simulations for cell 1 were carried out to investigate the effects of oxygen reactions on the cell performance during discharge. The oxygen evolution may take place during low rate discharge [4], where the potential of the positive electrode is higher than the equilibrium potential of the oxygen generation. The current produced by the oxygen evolution is opposite to the applied discharge current. As a result, the nickel active materials have to be overdischarged to produce an equal amount of the current in addition to the externally applied discharge current and the discharge efficiency (defined as the ratio of the charge output from the cell to the total charge consumption of the nickel active materials) is therefore less than 100%. A limiting case is the self-discharge of the Ni-MH cell [29, 30] in which the oxygen evolution causes a cell capacity loss. As the self-discharge proceeds, the potential of the nickel electrode decreases and finally goes below the equilibrium potential of the oxygen generation, and the self-discharge due to the oxygen evolution ceases. This trend is clearly shown by the self-discharge rate vs. time plot in Fig. 11. According to the simulation results, the cell loses its capacity quickly during the first 20 days due to the high potential of the nickel electrode and hence a high self-discharge rate. The residual capacity is reduced to below 60%. This value is too high compared to the experimental data (*ca.* 20%) [29, 30], pointing out that the exchange current density of oxygen generation during cell self-discharge used in the present simulation may not be realistic. Recent experimental studies [29, 30] indicated that the oxygen generation, or differently termed as the self-decomposition of the nickel active materials, yields the lowest rate of the self-discharge of the Ni-MH cell and the redox shuttle between nitrogen ions and ammonia can accelerate the self-discharge process. However, the latter mechanism caused by the decomposition of the conventional separator material in the electrolyte can be completely suppressed by a special design of the separator to trap the entire quantity of nitrogen impurities [29, 30]. Therefore, oxygen evolution remains to be a rate-limiting step of the self-discharge of Ni-MH batteries. Figure 12 shows the effects of oxygen evolution on the discharge efficiency and depth of discharge at various discharge rates. It is seen that the discharge efficiency is initially small when the cell discharges at small rates and increases as cell discharge proceeds. When the cell discharge rate is larger than C/1, the effect of oxygen evolution vanishes.

## CONCLUSIONS

A micro-macroscopic coupled model, that not only accounts for the proton diffusion in the nickel electrode and the hydrogen diffusion in the metal-hydride electrode but also incorporates oxygen reactions and transport through both electrolyte and gas phases, has been validated against discharge and charge experiments with good agreement. Numerical simulations have been performed to study the effects of oxygen reactions during charge and discharge. It is found that the charge acceptance decreases with the charge rate, while the depth of discharge increases and the initial discharge efficiency decreases with decreasing discharge rate. Oxygen evolving into the gas phase is responsible for the cell pressure build-up.

The present model assumed a continuous gas-pore network with a uniform volume fraction throughout the cell. In reality, however, the gas phase structure is dependent upon the oxygen-reaction and can be much more complex. Thermal effects on the performance of the Ni-MH cell, which are neglected in this work, can also be important at high-rate charge and discharge. In particular, the rate of oxygen generation increases very quickly with the cell temperature [12]. Future work will focus on integrating thermal modeling with the present electrochemical model accounting for the internal oxygen circulation.

Acknowledgments—This work was supported, in part, by the Defense Advanced Research Projects Agency (DARPA), Tactical Technology Office, Electric and Hybrid Vehicle Technology Program, under the cooperative agreement No. MDA972-95-2-0009.

## REFERENCES

1. T. Moore, "The road ahead for EV batteries," *EPRI Journal*, **March/April**, 7 (1996).
2. S.R. Ovshinsky, S.K. Dhar, S. Venkatesan, D.A. Corrigan, A. Holland, M.A. Fetcenko, and P.R. Gifford, "Ovanic Nickel Metal Hydride Technology for Consumer and Electric Vehicle Batteries — A Review and Up-date," in *Batteries for Potable Applications and Electric Vehicles* (edited by C.F. Holmes and A.R. Langrebe), The Electrochemical Society Proceedings Series, **PV 97-18**, p. 693 (1997).
3. T.F. Fuller and J. Newman, "Metal Hydride Electrodes," in *Modern Aspects of Electrochemistry*, R.E. White, J.O'M. Bockris, and B.E. Conway, editors, **27**, p.359 Plenum Press (1995).
4. D. Fan and R.E. White, "Mathematical Modeling of a Nickel-Cadmium battery — Effects of Intercalative and Oxygen Reactions," *J. Electrochem. Soc.*, **138**, 2952 (1991).
5. J.S. Newman, *Electrochemical System*, 2nd edition, Prentice Hall, Englewood Cliffs (1991).
6. B. Paxton and J. Newman, "Modeling of Nickel/Metal Hydride Batteries," *J. Electrochem. Soc.*, **144**, 3819 (1997).
7. W.H. Zhu, G.D. Zhang, D.J. Zhang, and J.J. Ke, "Gas Recombination in Sealed Ni-MH<sub>x</sub> Cells," *J. Chem. Tech. Biotechnol.*, **69**, 121 (1997).
8. C.Y. Wang, W.B. Gu, and B.Y. Liaw, "Micro-Macroscopic Coupled Modeling of Batteries and Fuel Cells Part I. Model Development," *J. Electrochem. Soc.*, **145**, 3407 (1998).
9. W.B. Gu, C.Y. Wang, and B.Y. Liaw, "Micro-Macroscopic Coupled Modeling of Batteries and Fuel Cells Part II. Application to Nickel-Cadmium and Nickel-Metal Hydride Cells," *J. Electrochem. Soc.*, **145**, 3418 (1998).
10. S.M. Li, *Numerical Simulation of Nickel-Metal Hydride Cells during Charge and Discharge*, M.S. thesis (Advisor: C.Y. Wang), University of Hawaii at Manoa, 1997.
11. T. Sakai, A. Takagi, K. Kinoshita, N. Kuriyama, H. Miyamura, and H. Ishikawa, "Influence of Binding Materials for Shaping Alloy Electrodes on the Performance of a Ni/Metal Hydride Battery," *Journal of the Less-Common Metals*, **172-174**, 1185 (1991).
12. D. Berndt, *Maintenance-Free Batteries*, 2nd edition, John Wiley & Sons (1997).
13. P. De Vidts and R.E. White, "Mathematical Modeling of a Nickel-Cadmium Cell: Proton Diffusion in the Nickel Electrode," *J. Electrochem. Soc.*, **142**, 1509 (1995).
14. P. De Vidts, J. Delgado, and R.E. White, R. E., "Mathematical Modeling for the Discharge of a Metal Hydride Electrode," *J. Electrochem. Soc.*, **142**, 4006 (1995).
15. R. Barnard, C.F. Randel, and F.L. Tye, *J. Applied Electrochem.*, **10**, 109 (1980).
16. M.S. Spritzer, *S-10344 NASA*, Technical Report (1977).
17. B.V. Ratnakumar, P. Timmerman, C. Sanchez, S.D. Stefano, and G. Halpert, "Predictions from the Macrohomogeneous Model of a Aerospace Ni-Cd Battery," *J. Electrochem. Soc.*, **143**, 803 (1996).
18. R. Zarzycki and A. Chacuk, *Absorption Fundamentals & applications*, Pergamon Press (1993).
19. D.M. Bernardi and M.K. Carpenter, "A Mathematical Model of the Oxygen-Recombination Lead-Acid Cell," *J. Electrochem. Soc.*, **142**, 2631 (1995).
20. J. Newman and W. Tiedemann, "Simulation of Recombinant Lead-Acid Batteries," *J. Electrochem. Soc.*, **144**, 3081 (1997).
21. T.V. Nguyen and R.E. White, "A Mathematical Model of a Hermetically Sealed Lead-Acid Cell," *Electrochimica Acta*, **38**, 935 (1993).
22. M. Micka and I. Rousar, *Electrochim. Acta*, **25**, 1085 (1980).
23. S.V. Patankar, *Numerical Heat Transfer and Fluid Flow*, Taylor & Francis (1980).
24. W.B. Gu, C.Y. Wang, and B.Y. Liaw, "Numerical Simulation of Coupled Electrochemical and Transport Processes in Lead-Acid Batteries," *J. Electrochem. Soc.*, **144**, 2053 (1997).
25. W.B. Gu, C.Y. Wang, and B.Y. Liaw, "The use of computer simulation in the evaluation of electric vehicle batteries," *J. Power Sources*, **75/1**, 154 (1998).

26. P.C. Milner and U.B. Thomas, "The Nickel-Cadmium Cell," in *Advances in Electrochemistry and Electrochemical Engineering*, P. Delahey and C.W. Tobias, editors, **5**, p.1, John Wiley & Sons (1967).
27. D. MacArthur, *J. Electrochem. Soc.*, **117**, 729 (1970).
28. R. Cates and R. Richey, "Charge Ni-Cd and Ni-MH batteries properly," *Electronic Design*, **44**, No. 12, Jun 10 (1996).
29. M. Ikoma, Y. Hoshina, I. Matsumoto, and C. Iwakura, "Self-Discharge Mechanism of Sealed-Type Nickel/Metal-Hydride Battery," *J. Electrochem. Soc.*, **143**, 1904 (1996).
30. P. Leblanc, Ph. Blanchard, and S. Senyarich, "Self-Discharge of Sealed Nickel-Metal Hydride Batteries Mechanisms and Improvements," *J. Electrochem. Soc.*, **145**, 844 (1998).

## List of Tables

Table I. Cell-specific parameters

Table II. Values of parameters for base case

Table I. Cell-specific parameters

Parameter	Cell 1	Cell 2 [14]
capacity of Ni electrode, Ah	1.0	30 (7 cells)
MH/Ni capacity ratio	1.7	2
specific charge capacity of MH powder, mAh/g	281	250
size of MH powder, $\mu\text{m}$	45	70
projected electrode area, $\text{cm}^2$	7.5×4.0	12×10
thickness, cm		
Ni electrode	0.07	0.079*
MH electrode	0.04	0.059*
separator	0.01	0.025*
electrolyte concentration, M	8	6
operating temperature, °C	25	24

\* — guessed from capacities

Table II. Values of parameters for the baseline case

Parameter	Value	Unit	Source
$D_e^{O_2}$	$5 \times 10^{-6}$	$\text{cm}^2/\text{s}$	[26]
$c_{\text{ref}}^{O_2}$	$1.0 \times 10^{-7}$	$\text{mol}/\text{cm}^3$	[4] [13]
$p_o^{O_2}$	$10^{-6}$	atm	chosen
H	$7.6 \times 10^{-8}$	$\text{mol}/\text{cm}^3 \cdot \text{atm}$	[26]
K	10	1/s	chosen
Ni electrode			
$\rho_{\text{avg}}$	3.55	$\text{g}/\text{cm}^3$	[6]
$c_{\text{max}}^H$	0.0383	$\text{mol}/\text{cm}^3$	$\rho_{\text{avg}}/M_{\text{Ni}(\text{OH})_2}$
$c_{\text{ref}}^H$	$0.5c_{\text{max}}^H$		chosen
$\epsilon_b$	0.85		[13]
$\epsilon_{\text{Ni}}$	0.39		calculated from capacity
$a_{sb}$	2000	$\text{cm}^2/\text{cm}^3$	[13]
$a_{\text{Ni}}$	4033	$\text{cm}^2/\text{cm}^3$	calculated from $a_{sb}$
$r_o$	$1.5 \times 10^{-4}$	cm	calculated from $a_{sb}$
$r_{\text{Ni}}$	$3.0 \times 10^{-4}$	cm	calculated from $a_{\text{Ni}}$
$i_{o1,\text{ref}}$	$1.04 \times 10^{-4}$	$\text{A}/\text{cm}^2$	[6]
$i_{o2,\text{ref}}$	$1 \times 10^{-11}$	$\text{A}/\text{cm}^2$	[4] [13]
$\alpha_{a1}$	0.5		[13]
$\alpha_{c1}$	0.5		[13]
$\alpha_{a2}$	1.5		[4] [13]
$\alpha_{c2}$	0.5		[4] [13]
k	0.789		[16]
$D^H$	$4.6 \times 10^{-11}$	$\text{cm}^2/\text{s}$	[27]
Separatior			
$\epsilon_s$	0.68		[13]

Table II. Parameters used in simulations (cont'd)

Parameter	Value		Unit	Source	
MH electrode	Cell 1	Cell 2 [11]		Cell 1	Cell 2 [11]
$\rho_{\text{avg}}$	7.49		$\text{g/cm}^3$	[6]	
$c_{\text{max}}^{\text{H}}$	0.1025	0.0912	$\text{mol/cm}^3$	$\rho_{\text{avg}}/M_{\text{LaNi}_5\text{H}_6}$	$\rho_{\text{avg}}/M_{\text{AB}_5\text{H}_6}$
$c_{\text{ref}}^{\text{H}}$	$c_{\text{max}}^{\text{H}}$			chosen	
$\epsilon_{\text{MH}}$	0.48			calculated from capacity	
$r_{\text{MH}}$	22.5	35	$\mu\text{m}$	measured	
$a_{\text{MH}}$	693	446	$\text{cm}^2/\text{cm}^3$	calculated from $\epsilon_{\text{MH}}$ and $r_{\text{MH}}$	
$i_{\text{o3,ref}}^{\text{H}}$	$3.2 \times 10^{-4}$	$7.85 \times 10^{-4}$	$\text{A/cm}^2$	fitted	[6]
$i_{\text{o4,ref}}^{\text{H}}$	$1 \times 10^{-14}$		$\text{A/cm}^2$	[4] [13]	
$\alpha_{\text{a3}}$	0.5			[4] [13]	
$\alpha_{\text{c3}}$	0.5			[4] [13]	
$\alpha_{\text{a4}}$	1.5			[4] [13]	
$\alpha_{\text{c4}}$	0.5			[4] [13]	
$p$	0.167			chosen	
$D^{\text{H}}$	$2.0 \times 10^{-8}$		$\text{cm}^2/\text{s}$	[6]	

## List of Figures

- Figure 1. A schematic diagram of a Ni-MH cell and the model representation
- Figure 2. Comparison of predicted cell discharge potential (solid lines) with experimental results (symbols)
- Figure 3. Comparison of predicted cell potential (solid lines) with experimental results (symbols, Sakai et al., 1991): (a) discharge and (b) charge
- Figure 4. State of charge of the Ni-MH cell during 2C charge at various exchange current densities of the oxygen generation reaction
- Figure 5. Charge potential curves of the Ni-MH cell during 2C charging at various exchange current densities of the oxygen generation reaction: (a) cell potential vs. charge input and (b) cell potential vs. state of charge
- Figure 6. Cell pressure profiles during 2C charging at various exchange current densities of the oxygen generation reaction
- Figure 7. Effect of oxygen reactions on the Ni-MH cell performance at various charging rates: (a) state of charge vs. charge input and (b) cell potential vs. state of charge
- Figure 8. Charge acceptance vs. state of charge of the Ni-MH cell at various charging rates as a result of oxygen reactions
- Figure 9. Cell pressure profiles of the Ni-MH cell at various charging rates
- Figure 10. Effect of the interfacial mass transfer coefficient on the cell pressure variation during C/1 charging
- Figure 11. Cell potential, self-discharge rate, and residual capacity vs. time curves of the Ni-MH cell as a result of oxygen reactions
- Figure 12. Effect of oxygen generation on the discharge efficiency and depth of discharge of the Ni-MH cell at various rates